The temperature dependence of thermal conductivity for lherzolites from the North China Craton and the associated constraints on the thermodynamic thickness of the lithosphere

Sheqiang Miao,[1,2] Heping Li[1] and Gang Chen[1,2]

[1]*Laboratory for High Temperature and High Pressure Study of the Earth's Interior, Institute of Geochemistry, Chinese Academy of Sciences, Guiyang* 550002, *China.* E-mail: *Lihp0803@163.com*
[2]*University of Chinese Academy of Sciences, Beijing* 100049, *China*

SUMMARY

In this study, the authors aimed to compute the lithospheric thickness beneath the North China Craton (NCC) by combining the measurement of the thermophysical properties of lherzolite xenoliths from the Cenozoic basalts in North China with the corresponding geothermal data, thus providing geothermal constraints for the lithospheric thinning beneath the NCC. Based on the precise measurement of the thermal diffusivity, specific heat capacity at high temperatures, and density at room temperature for lherzolites from the NCC, the temperature dependence of lattice thermal conductivity for lherzolites was obtained. Combining with the surface heat flow, heat production of rocks and other relevant conditions, the average thickness of the lithosphere beneath the NCC and the lithospheric thickness of secondary massifs were computed, and we identified the relationship between depth and temperature beneath the NCC and each secondary massif. The computed lithospheric thickness is highly consistent with the results of geophysical observations. The computation results of this study indicate that the average lithospheric thickness of the current NCC and the average thickness of the eastern NCC were 101 and 75 km, the lithospheric thickness of the Ordos block increases from 110 km in the east to approximately 200 km in the west, and the average thickness is 141 km, that were thinner than that in the Archean era (200 km) by approximately 100, 125 and 60 km. These results reveal that, in addition to eastern NCC, the Taihang orogenic belt and Ordos block have also experienced varying degrees of thinning with a thinning centre oriented in the north–south direction, consistent with the direction of the thinning centre along the Tanlu fault zone beneath the east NCC.

Key words: Numerical solutions; Heat flow; Cratons; Heat generation and transport; Asia.

1 INTRODUCTION

A craton is a portion of the continental crust that formed prior to the Archean era, and its genesis, similar to the oceanic crust, is related to the basalt that was generated by partial melting of the upper mantle. However, due to its low density and the presence of a thick lithosphere underneath, a craton is difficult to destroy by subduction post-formation. Effectively, cratons have not experienced either magmatic or tectonic activity; additionally, no significant seismic activity occurs in these regions. Therefore, cratons have existed stably for over 2.5 billion years and are the most stable regions on Earth.

However, the North China Craton (NCC) exhibits some characteristics that are distinctly different from other cratons in the world. After its formation and until the Archean era, the NCC was relatively stable; however, studies of the structural geology, geochem-istry and geophysics of mantle xenoliths indicate that the NCC has experienced a strong modification since the Mesozoic era (Griffin *et al.* 1998; Fan *et al.* 2000; Xu 2001; Gao *et al.* 2002; Deng *et al.* 2007). From the geothermal perspective, cratons generally have a relatively low surface heat flow and are consistent in lithsopheric temperatures and thickness (Rudnick *et al.* 1998). In the cratons that formed early, the surface heat flow was relatively small due to the depletion of heat-producing elements (such as uranium, thorium and potassium). For example, the average surface heat flow of the Canadian Shield and the Siberian Shield are 42 and 35 mWm^{-2} (Jaupart *et al.* 1998). However, the average surface heat flow of the NCC is up to 60 mWm^{-2}, and in the eastern region, the heat flow reaches values as high as 68 mWm^{-2} (Wang & Huang 1990; Hu *et al.* 2000). This comparatively high surface heat flow anomaly in comparison to other cratons also indicates that the lithosphere of North China most likely experienced a strong modification.
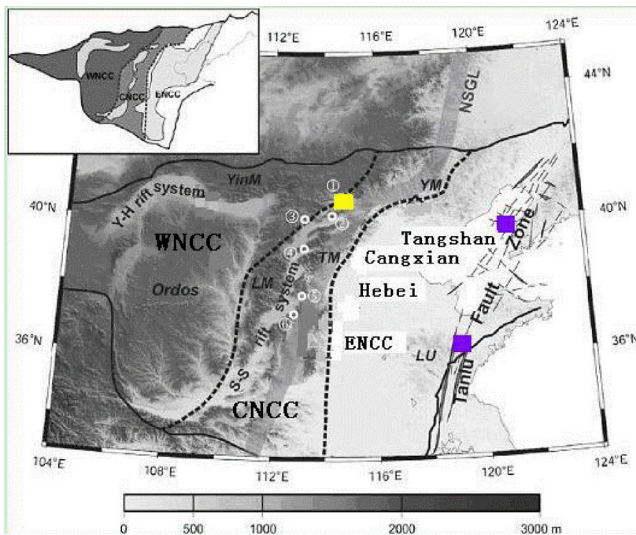
Figure 1. Topographic map of the North China Craton (after Chen *et al.* 2009). The purple box shows the output location of Palaeozoic kimberlite xenoliths, the yellow box shows the output location of Cenozoic basalt xenoliths. The sample was collected from location ①. NSGL, north–south gravity lineament; ENCC, eastern north China craton rift; Lu, Luxi uplift; Tangshan, Tangshan earthquake region; Hebei, Hebei depression; Cangxian, Cangxian uplift; YM, Yan Mountains; YinM, Yin Mountains; TM, Taihang Mountains; LM, Lvliang Mountains; Ordos, Ordos block; Y-H rift system, Yinchuan-Hetao rift system; S-S rift system, Shanxi-Shanxi rift system.

In this paper, we aim to calculate the lithospheric thickness beneath the NCC by measuring the thermal conductivity of upper mantle rocks of NCC and by combining with the geothermal data to provide geothermal constraints for the lithospheric thinning beneath the NCC.

Lherzolite is one of the most important rock types known in the upper lithospheric mantle beneath the NCC area and generally appears as xenoliths in Cenozoic basalts. It is believed to be a newly formed lithospheric mantle after the Mesozoic thinning event and is representative of lithospheric mantle rocks in the mid-eastern region (Fan & Hooper 1989; Chi & Yan 1998; Fan *et al.* 2000). No magmatic activity occurred in the Ordos region in the west NCC after craton formation due to the stable tectonic activity, and thus the deep rock cannot outcrop on the surface. However, scholars generally consider the highly depleted harzburgite of the Palaeozoic kimberlitic xenoliths in the eastern region (such as Fuxian County and Mengyin County) to be the main rock type in the upper mantle lithosphere of the Ordos block, whereas the central orogenic belt is a mixture of lherzolite and harzburgite (Qiu *et al.* 2005). The locations of lherzolite and harzburgite are shown in Fig. 1.

Many methods are available for the measurement of the heat transfer properties of materials under high temperatures, among which the laser-flash technique proves superior. Laser-flash technique is a non-contact method of measurement capable of avoiding contact thermal resistance, which cannot be eliminated in the conventional contact measurement method. Meanwhile, the direct radiative transfer under high temperature can be inhibited by spraying carbon and metal films on the surface of samples, which benefits the measurement of the actual lattice thermal conductivity of samples (Hofmeister 2006). This method directly measures the thermal diffusivity of samples and calculates the thermal conductivity using the specific heat capacity and density of samples. Because this method only involves one sample parameter (i.e. thickness), the accuracy

for thermal diffusivity is relatively high, with a nominal error of 3 per cent.

Using this laser-flash technique, thermal diffusivities for many rock-forming minerals have been measured, for example, olivine, pyroxene and garnet (Hofmeister 2006, 2012; Pertermann & Hofmeister 2006; Hofmeister & Pertermann 2008). Thermal diffusivity for rocks have also been determined more recently (Nabelek *et al.* 2010; Romine *et al.* 2012). Merriman *et al.* (2013) using the measurement results modelled the present-day thermal structure of Archean cratons as a function of crustal lithological structure.

In this study, we attempted the use of the laser-flash method to measure the thermal diffusivity of lherzolite under conditions ranging from room temperature to 1200 °C. Additionally, heat-flow differential scanning calorimetry was applied to acquire the specific heat capacity of the rock type under different temperatures, and a push-rod dilatometer was used to measure the expansion coefficient in the corresponding temperature range. The density parameter of rocks under normal temperature was then incorporated to calculate the thermal conductivity of lherzolite under conditions ranging from room temperature to 1200 °C. Eventually, the surface heat flows were incorporated to calculate the lithospheric thickness distribution and depth-temperature profile beneath the NCC.

2 EXPERIMENTS

2.1 Sample characteristics

The lherzolite samples were collected at Damaping of Zhangjiakou, Hebei Province, and are Cenozoic basalt xenoliths. The specimens appeared pale green without crack development. In this study, the density of the samples was measured under ambient condition, based on Archimedes' principle, yielding the value 2.26 g cm^{-3}.

A representative optical micrograph is shown in Fig. 2. Microscopic observations indicated that the sample was mainly composed of olivine and pyroxene, with a granular mosaic structure and an average particle size of 0.5 mm. The sample contained 55 per cent olivine (volumetric fraction, hereinafter), 22 per cent orthopyroxene, 20 per cent clinopyroxene, 3 per cent spinel and a little serpentine.

The chemical compositions of the rock and its main constituent minerals are shown in Table 1.
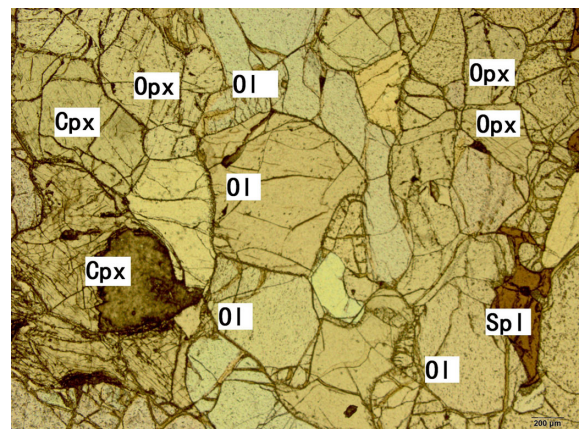

Figure 2. Photomicrograph of lherzolite under plane-polarized light. OI, olivine; Cpx, clinopyxene; Opx, orthopyroxene; Spi, chrome spinel.

Table 1. Chemical compositions of the rock and its main constituent minerals (wt per cent).

Oxides	SiO$_2$	TiO$_2$	Al$_2$O$_3$	FeO*	MnO	CaO	Na$_2$O	K$_2$O	P$_2$O$_5$	CO$_2$	MgO	Cr$_2$O$_3$	Total
Rock	46	0.05	2.43	7.36	0.15	2.56	0.24	0.01	0.02	4.10	36.43	–	99.35
OI	42.24	0.02	0.28	8.64	0.19	–	–	–	–	–	48.71	0.07	100.15
Cpx	53.35	0.81	5.16	4.36	0.09	21.6	1.74	–	–	–	13.18	0.58	100.87
Opx	54.88	–	3.58	10.99	0.06	0.51	0.04	0.04	–	–	29.69	0.22	100.01
Cr	–	–	23.46	24.55	–	0.04	–	–	–	–	9.95	40.06	98.06

Notes: OI, olivine; Cpx, clinopyroxene; Opx, orthopyroxene; Cr, chrome spinel; FeO*, whole iron; –, no detection. Analytical method for rock was X-ray fluorescence analysis, for minerals was electron microprobe analysis.
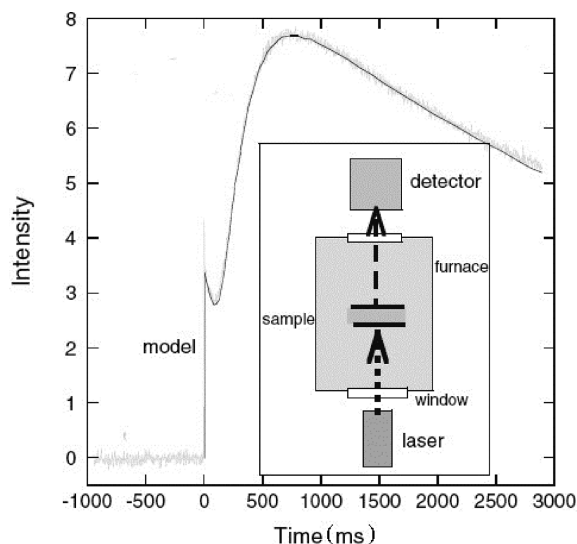
Figure 3. The essentials of laser-flash measurements (after Hofmeister 2006).

2.2 Measurement of the thermal diffusivity

Fig. 3 shows a schematic diagram for LFA427 (Hofmeister 2006). The disk-shaped sample, 12.70 mm in diameter and 2.50 mm thick, is coated with metal and graphite for suppressing the direct radiative transfer at high temperature and placed within the furnace chamber, and then the chamber is filled with Ar gas. The sample is mounted on a carrier system which is located in a furnace. After the sample reaches a predetermined temperature, a burst of energy emanating from a pulsed laser is absorbed on the front face of the sample, resulting in homogeneous heating. The relative temperature increase on the rear face of the sample is then measured as a function of time by an IR detector. Based on the Cowan's model,

$$D = 0.1388 \times l^2/t^{0.5}, \tag{1}$$

the thermal diffusivity D can be calculated. Here, l is the thickness of the sample, and $t_{0.5}$ is the time taken by the rear surface of the sample to reach half of the highest temperature.

2.3 Measurement of the specific heat capacity and thermal expansion coefficient

The specific heat capacity of the samples was measured with a STA449C simultaneous thermal analyser, which was made based on the principle of heat flow differential scanning calorimetry (DSC; Hirono & Hamada 2010). The heating rate was 20 °C min^{-1}, and the temperature range was 27 to 1200 °C. The entire heating process was implemented under heat flow with inert argon gas. Using this apparatus, this study also obtained the thermogravimetry (TG) data.
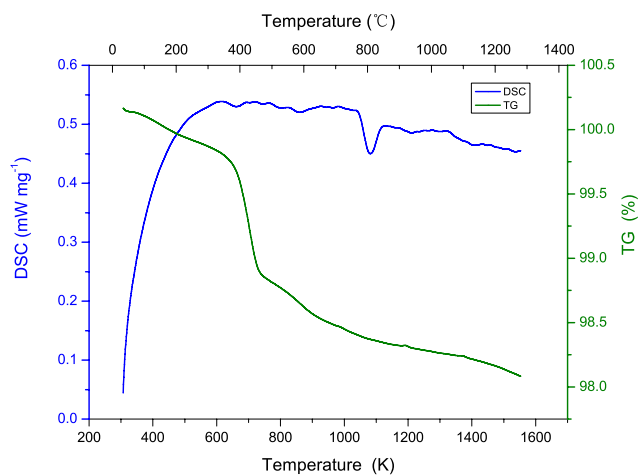
Figure 4. The DSC and TG curves for lherzolite.

The thermal expansion coefficient of each sample under high temperature was measured with a DIL 402 PC pushrod thermal dilatometer (Shen *et al.* 2009). The heating rate was 5 °C min^{-1}, and the measurement range was 30–1250 °C. The inert gas was nitrogen.

3 RESULTS AND DISCUSSION

3.1 Specific heat capacity

As temperature increasing, the DSC signals and weight-loss information for the sample are shown in Fig. 4.

As shown in Fig. 4, significant weight loss occurs at 400–500 °C for the TG curve, indicating a decomposition reaction, that is, that the serpentine is dehydrated with interlay water. The DSC signal has a strong exothermic peak at 810 °C, which could be caused by recrystallization of forsterite and enstatite (Gualtieri *et al.* 2012; Seipold & Schilling 2003). The weight lost by the samples was approximately 1.8 per cent during the entire heating interval.

Fig. 5 shows the derived results for the specific heat capacity. Using 810 °C as the boundary, we fit the results piecewise according to the equation (Saxena 1996):

$$C_P = a + bT + cT^2 + dT^{-2} + eT^{-1}, \tag{2}$$

where the unit of T is Kelvin. The fitting parameters are shown in Table 2.

3.2 Thermal expansion and density change

The measurement results for the thermal expansion of the samples are shown in Fig. 6. As can be observed from the Fig. 6, sample length increases linearly with increasing temperature. In the
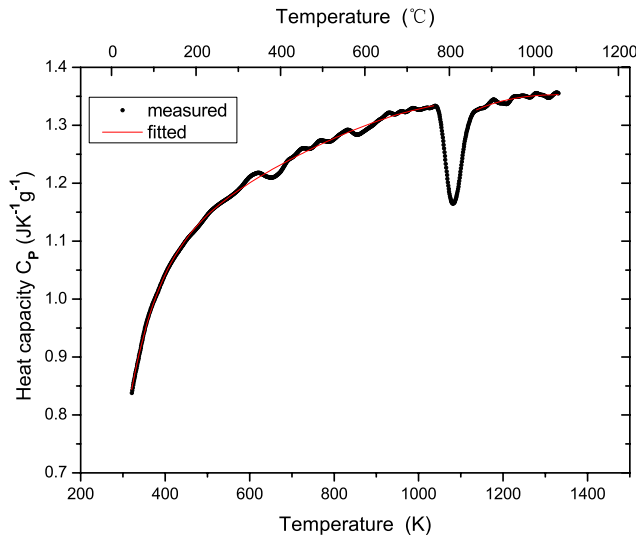
Figure 5. The temperature dependence of the specific heat capacity of lherzolite.

Figure 6. Curve of the temperature dependence of linear expansion and density.

temperature range of 30–1250 °C, as covered in the experiment, the length increased by 1.58 per cent, and the volume expanded by 4.74 per cent. Calculated sample density decreases linearly with increasing temperature.

3.3 Thermal diffusivity and thermal conductivity

Based on the precise measurement of the thermal diffusivity, specific heat capacity, thermal expansion coefficient and TG at high temperatures conditions for lherzolites, the temperature dependence of lattice thermal conductivity for lherzolites was calculated as

$$k = \rho D C_P. \tag{3}$$

The temperature dependence of thermal diffusivity and thermal conductivity for lherzolite are shown in Fig. 7, where thermal diffusivity was fitted to $D = a + b/T + c/T^2$, and thermal conductivity was fitted to $k = e + fT + gT^2$ (Pertermann *et al.* 2008). The unit of T is Kelvin, and the fitting results are $a = 0.36579$, $b = 76.8194$, $c = 5.90405 \times 10^4$ and $R^2 = 0.975$ for thermal diffusivity; $e = 4.31528$, $f = -0.00359$, $g = 1.3086 \times 10^{-6}$ and $R^2 = 0.97206$ for thermal conductivity.

As shown in Fig. 7, the thermal diffusivity of lherzolite, as obtained in this experiment, is significantly lower than that of its constituent components, forsterite crystal (Pertermann & Hofmeister 2006); additionally, it is lower than that of forsterite aggregate with 5 per cent diopside/enstatite (Katsura 1995). This result is close (slightly higher) to that of lherzolite, as measured by Gibert *et al.* (2003). Additionally, it is within the range of thermal diffusivity of the anisotropic mantle lherzolite (74 per cent olivine, 18 per cent enstatite, 6 per cent diopside and 2 per cent spinel) and harzburgite (87 per cent olivine, 12 per cent enstatite and 1 per cent spinel) derived by Tommasi *et al.* (2001) using the hot-wire method. Because
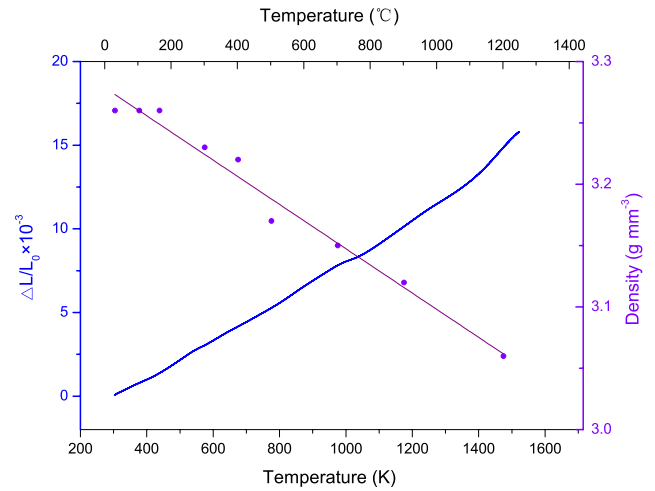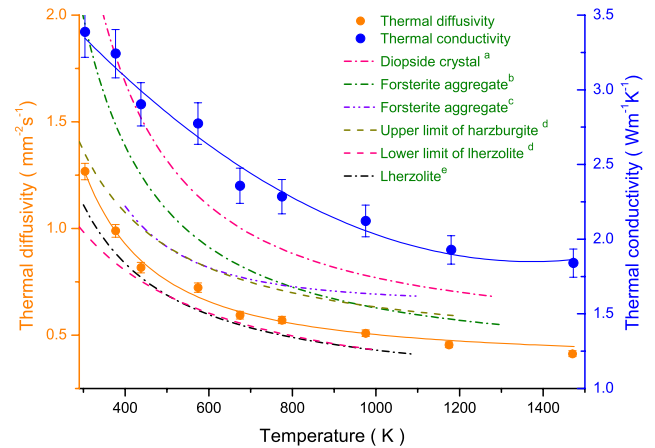

Figure 7. Comparison of thermal diffusivity for lherzolite with previous works and calculated thermal conductivity. [a]Hofmeister & Pertermann (2008) [Ca$_{1.01}$(Mg$_{0.923}$Fe$_{0.053}$Mn$_{0.009}$)Si$_2$O$_6$], [b]Perterman & Hofmeister (2006) Forsterite (Mg$_{1.8}$Fe$_{0.2}$SiO$_4$) + 5 per cent pyroxene aggregate, [c]Katsura (1995) Forsterite (Mg$_{1.8}$Fe$_{0.2}$SiO$_4$) + 5 per cent enstatite aggregate, [d]Tommasi *et al.* (2001), [e]Gibert *et al.* (2003) lherzolite (75 per cent olivine, 18 per cent enstatite, 5 per cent diopside).

of the lower content of olivine, the thermal diffusivity of the lherzolite measured in this experiment is relatively closer to the lower limit of Tommasi's results.

The lherzolite result is lower than the constituent crystal due to the existence of porosity in the rocks; additionally, the contained microcracks, grain boundaries have a phonon-scattering effect, leading to the relatively low thermal diffusivity (Smith *et al.* 2003; Poulier *et al.* 2007; Zivcova *et al.* 2009).

Table 2. Fitting parameters of specific heat capacity.

	a	b	c	d	e
25–770 °C	−1.4336	2.8100×10^3	-9.6653×10^{-7}	-2.0962×10^5	1.1265×10^3
870–1060 °C	−65.018	3.5000×10^2	-7.0390×10^{-6}	-1.8449×10^7	5.6668×10^4

Table 3. Average crustal layering and parameters of North China Craton crust (after Chi & Yan 1998). $k_{P,T}$ can get from eq. (7).

Layer	Thickness, Z (km)	Thermal conductivity, k (Wm^{-1}k^{-1})	Heat production, A (μWm^{-3})	Heat flow on the top, q_T (mWm^{-2})
Sedimentary cover	3	2.2	1.08	60
Basement	12	3.0	1.25	57
Middle crust	10	2.8	0.84	42
Lower crust	13	2.6	0.32	34
Lithospheric mantle		$k_{P,T}$	0.03	30

4 CALCULATION OF THE LITHOSPHERIC THICKNESS AND TEMPERATURE-DEPTH RELATIONSHIP BENEATH THE NCC

4.1 Computation procedure

1-D steady-state conductive geotherms are computed using a bootstrapping method (Chapman 1986), which requires thermal conductivity, surface heat flow and heat production rate as inputs. The vertical column is divided into arbitrarily thin layers, for which properties can be considered constant. Temperature, T_B, and heat flow, q_B, at the bottom of each layer are determined from the temperature, T_T, and heat flow, q_T, at the top of each layer by

$$T_B = T_T + \frac{q_T}{k} \times \Delta z - \frac{A \Delta z^2}{2k}, \tag{4}$$

and

$$q_B = q_T - A \times \Delta z, \tag{5}$$

where A and k are the intralayer heat production and conductivity, respectively (Chapman 1986). The layer thickness is given by Δz and set to 10 m. We adopt the mantle adiabat as

$$T_m = 1300\,^\circ C + 0.4\,z, \tag{6}$$

where z is depth (km), which is uniform on the global scale (Thompson 1992).

The temperature–depth relationship in the crust is calculated using the stratified crust model established by Chi & Yan (1998) (include stratification, thermal conductivity and heat production), as shown in Table 3.

4.2 Selection of the input parameters

4.2.1 Thermal conductivity

In previous works, due to the lack of precise information on the relationship between thermal conductivity and temperature of the upper-mantle rocks, authors always used a fixed value of thermal conductivity (Jaupart *et al.* 1998; Artemieva & Mooney 2001). Other scholars used a functional relationship between thermal conductivity and temperature (Zang *et al.* 2002; Wang & Cheng 2012).

Due to its increased contribution to heat transfer under high temperature, radiative heat conduction was included in our computation. The authors have used one of the most popular formulations, as derived by Hofmeister (1999).

We took into account the influence of pressure on the lattice thermal conductivity, which is roughly $k^{-1} \partial k / \partial P = 0.04$ GPa^{-1} for olivine (Osako *et al.* 2004; Xu *et al.* 2004); accordingly, the pressure effect might be even larger for pyroxene (Hunt *et al.* 2011), however, we still adopt 0.04 GPa^{-1} as the pressure coefficient of lherzolite as an approximation. The total thermal conductivity,

$$k_{P,T} = (4.31528 - 0.00359T + 1.3086 \times 10^{-6}T^2)$$
$$\times (1 + 0.04 \times z/30) + k_{rad}, \tag{7}$$

where $k_{rad} = 0.01753 - 0.00010365T + 2.2451T^2 \times 10^{-7} - 3.407T^3 \times 10^{-11}$, z is depth (km), the unit of T is Kelvin.

It is worth noting that, for the Ordos region, the upper mantle lithosphere mainly consists of harzburgite (Qiu *et al.* 2005), which is rich in Mg and poor in Fe, displaying a thermal conductivity value higher than that of lherzolite by approximately 20 per cent under the same temperature (Tommasi *et al.* 2001). As for the central Taihang orogenic belt, we used a thermal conductivity that is 1.1-fold that of lherzolite for the upper mantle rocks in this region as an approximation.

4.2.2 Surface heat flow

In China, measurements of the surface flow began in the 1960s; to date, there have been approximately 900 measurement sites located on the mainland of China. However, the distribution of these measurement sites is not uniform. For example, for NCC, the measurement sites are mostly concentrated in the east basin area surrounding the Bohai Sea, and there are some high-quality measurement sites in the Taihang Mountains and mid-south of the Ordos. However, there is a lack of measurement sites in the Yanshan Mountains, the Yinshan Mountains, and the north of the Ordos.

Based on the data from the existing measurement sites, the surface heat flow is highest, approximately 70 mWm^{-2}, in the eastern and central rift basins in NCC, and 60 mWm^{-2} in Taihang Mountains. In the Ordos, the surface heat flow decreases from 65 to 55 mWm^{-2} from east to west (Wang & Huang 1990; Hu *et al.* 2000, 2001). The average surface heat flow density of the NCC is 60 mWm^{-2}.

4.2.3 The heat production of crust and mantle

Nearly three decades ago it was discovered that surface heat flow correlates positively with heat production in particular heat flow provinces (Lachenbruch 1968; Roy *et al.* 1968):

$$q_s = q_r + GA, \tag{8}$$

where q_s is the surface heat flow, q_r is the reduced heat flow, G is the slope of the line and broadly reflects the depth distribution of heat producing elements and A is the heat production at the surface.

However, recent work has shown that such an interpretation is likely to be in error (Furlong & Chapman 1987; Pinet & Jaupart 1987; Nyblade & Pollack 1993). Some constraints on vertical heat production variation come from deep boreholes and exposed crustal cross-sections (Ketcham 1996; Forster & Forster 2000; Brady *et al.* 2006; He *et al.* 2008; Roy *et al.* 2008). However, these observations also show little correlation of heat production with depth. Given the poor correlation of heat production with depth in the crust, we

adopt constant heat production for each layer (Hasterok & Chapman 2011).

The upper crust in North China is composed of post-Archean granite and granodiorite, and the middle and lower crusts are composed of Archean TTG, diorite, and amphibolites rocks (Chi & Yan 1998). Chi & Yan (1998) conducted a large number of detailed measurements of the heat production rate of rocks with varying lithologies in the NCC. They derived the heat production of the upper, middle, lower crustal rocks and the sedimentary cover as 1.08, 1.25, 0.84 and 0.32 μWm^{-3}, respectively.

The heat production of the lithospheric mantle is very low relative to the crust, about 0.02 μWm^{-3} for depleted mantle <200 km and 0.045 μWm^{-3} for the mantle at 200–450 km (Chapman 1986; Furlong & Chapman 2013). We used 0.03 μWm^{-3} as the heat production of the upper mantle, which, as shown later in the analysis, does not significantly affect the results.

Based on the discussion presented above, the parameters that were eventually used in the calculation of the average lithospheric thickness beneath the NCC and the temperature–depth relationship are shown in Table 3.

4.3 The average lithospheric thickness beneath the NCC and the depth–temperature relationship

The computation results of the average lithospheric thickness beneath the NCC and the temperature–depth profile for different surface heat flows are shown in Fig. 8, where the abscissa of the intersection of the geoisotherm and the mantle adiabatic line indicates the thickness of the lithosphere corresponding to this surface heat flow density. Additionally, as indicated by the black solid line in Fig. 8, the average crustal thickness beneath the NCC is 38 km (Ma *et al.* 1991; Huang & Zhao 2004; Li *et al.* 2006), and the ordinate intersection points with each geo-isotherm indicate the Moho temperature. The results shown in the Fig. 8 are summarized below.

(1) As the surface heat flow decreases, the lithospheric thickening caused by the unit heat flow reduction becomes more significant, whereas the amplitude of the decrease in the Moho temperature remains essentially the same.

(2) The average surface heat flow of 60 mWm^{-2} in the NCC (Wang & Huang 1990; Hu *et al.* 2000) correspondingly indicates an average lithospheric thickness of 101 km, which is consistent
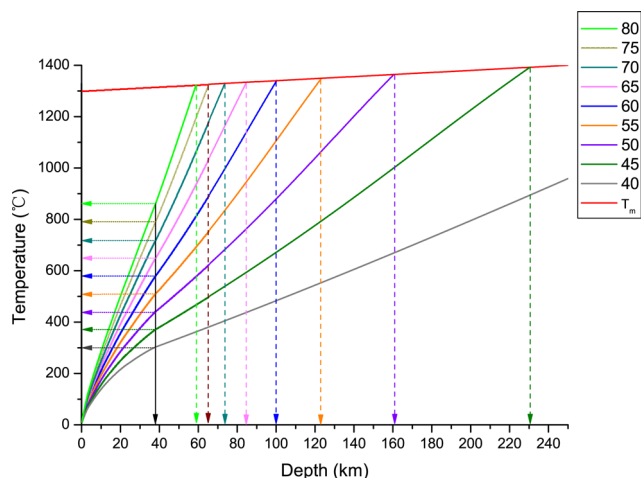

Figure 8. Depth–temperature relation of the NCC with different surface heat flow. Numbers were surface heat flow density, T_m was the mantle isentrope.

with the results from the geophysical observations (Chen *et al.* 2006; Xu & Zhao 2009; Chen 2010).

4.4 Analysis of the influential factors

Table 4 shows the effect of various factors on the calculation of temperature variation and lithospheric thickness. As shown in Table 4, the surface heat flow is the main factor that dominates the results of the computation, followed by thermal conductivity of the upper mantle and heat production of the upper crust, which has been referred to in previous analyses (Hasterok & Chapman 2011). The thickness of upper crust, heat production of middle and lower crust, the longitudinal distribution of heating elements inside the crust and thermal conductivity of the crustal rocks are also important factors that affect the results. The heat production of the upper mantle has the least significant impact. In regions with different surface heat flows, effects of various factors on computed results were different, which was not shown in Table 4 since the difference was not that great.

4.5 The lithospheric thickness of secondary massif

In the calculation, the crustal stratification and thickness of individual secondary massifs refer to the studies by previous seismological observations (Ma *et al.* 1991; Jia & Zhang 2005; Li *et al.* 2006; Zheng *et al.* 2007, 2011). The surface heat flows for individual secondary massifs refer to the data provided by Wang & Huang (1990), Hu *et al.* (2000, 2001). The radiogenic heat production and thermal conductivity for each layer refer to the data provided by Chi & Yan (1998), which were list in Table 3. The computation results for the lithospheric thickness of individual secondary massifs beneath the NCC are listed in Table 5. Because the Moho depth is different for different massifs, the temperature at 30 km of depth was used to compare the degree of hotness and coldness in different lithospheres. The error was obtained from analysis of the influential factors as shown in Table 4. The thickness of upper and lower crust was precise enough because it comes from seismic velocity observation, so the main error comes from the accuracy of surface heat flow, heat production of the crust and thermal conductivity of upper mantle. We assume that the uncertainty for heat flow was 5 per cent, for heat production of the crust was 20 per cent, for thermal conductivity was 7 per cent. The overall error for each subblocks were list in Table 5.

4.5.1 Rift basins in the east of NCC

For depressions, in this paper, we only provide related results for the Hebei depression. These results are similar to the results obtained for other depressions in the studied region.

Compared to the Hebei depression, the surface heat flow is relatively high in the Tangshan earthquake region, where the lithosphere is relatively thin. For the Cangxian uplift, because the sedimentary cover is relatively thin and the heating elements are concentrated underneath, the lithosphere is relatively thick.

4.5.2 Taihang uplift belt

The average surface heat flow for Taihang uplift zone is 59 mWm^{-2} (Hu *et al.* 2000). After a 10 per cent correction to the thermal conductivity data, we obtained the average thickness of the Taihang lithosphere as 121 km.

Table 4. Parameter sensitivities for geothermal calculations.

Parameter	Value	Perturbation (per cent)	Lithospheric thickness (per cent)
Heat flow	50 mWm^{-2} (shield)	+10	−25
	70 mWm^{-2} (rift)	+10	−16
Heat production			
Upper crust	1.2 μWm^{-3}	+20	+13
Middle crust	0.8 μWm^{-3}	+20	+6
Lower crust	0.3 μWm^{-3}	+20	+3
Upper mantle	0.03 μWm^{-3}	+20	+1
Thickness			
Upper crust	12 km	+10	+5
Lower crust	13 km	+10	+1
Thermal conductivity			
Upper crust	3.0 Wm^{-1}K^{-1}	+10	+2
Lower crust	2.6 Wm^{-1}K^{-1}	+10	+1
Upper mantle	k_{m}	+10	+7

Table 5. Crustal thickness of subblocks and its layered approach for calculation and the calculated results.

		$q_0{}^a$	S^b	B^b	MC^b	LC^b	TC^b	T_{30km}	T_{moho}	q_r	L	M (5 per cent)	M (10 per cent)	M (20 per cent)	Error
ENCC	HB	68	6	9	10	5	30	616	616	40.27	73	–	–	–	±17
	CX	68	3	12	11	7	33	567	612	38.28	79	–	–	–	±19
	TS	70	2	14	9	8	33	616	667	40.22	72	–	–	–	±17
Taihang		59	2	13	10	17	42	464	597	26.75	113	116	121	–	±30
		55						422	535	22.75	137	140	149	–	±35
S-S rift		73	3	12	10	13	38	623	763	43.00	68	69	71	–	±17
Ordos		65	4	15	10	15	44	528	696	28.73	98	–	104	110	±26
		60						474	614	23.73	123	–	132	141	±35
		55						420	533	18.73	166	–	182	198	±50

Notes: No modification for ENCC, for Taihang and S-S Rift were 5 per cent and 10 per cent; for Ordos, it was 20 per cent. q_0, surface heat flow (mWm^{-2}); S, sedimentary cover thickness (km); B, basement thickness (km); MC, middle crust thickness (km); LC, lower crust thickness (km); TC, total crust (km); T_{30km} (°C); T_{moho} (°C); q_r, reduced heat flow (mWm^{-2}); L, lithosphere thickness (km); M, modification (km); Error (km). ENCC, eastern North China craton; HB, Hebei depression; CX, Cangxian uplift; TS, Tangshan earthquake region; Taihang, Taihang orogenic belt; S-S rift, Shanxi-Shanxi rift; Ordos, Ordos block.
[a]Wang & Huang (1990) and Hu *et al.* (2000, 2001).
[b]Ma *et al.* (1991), Jia & Zhang (2005), Li *et al.* (2006) and Zheng *et al.* (2007, 2011).

At the junction of the Yanshan Mountains and Taihang Mountains in the northwest of Beijing, the average heat flow is approximately 55 mWm^{-2} and the derived lithospheric thickness is 149 km, consistent with the results of Chen *et al.* (2008).

As for the Shanxi-Shanxi rift, because the surface heat flow is abnormally high, reaching 73 mWm^{-2}, the calculated lithospheric thickness is relatively thin, approximately 70 km.

4.5.3 Ordos block

In the Ordos block, for longitudes ranging from 110° to 106°, namely, from the northeast to the southwest, the surface heat flow decreases from approximately 65 Wm^{-2} to approximately 55 mWm^{-2} with an average of 60 mWm^{-2} (Wang & Huang 1990). After correction for thermal conductivity, we derived that the lithospheric thickness beneath the Ordos block, which increases from 110 km in the northeast to 198 km in the southwest with an average lithospheric thickness of 141 km. Huang & Zhao (2006) studied the velocity characteristics in the cross-section of the east–west direction across the middle of NCC and found that the lithospheric thickness in the Ordos region increases from 110 km in the east to 200 km in the west, consistent with the results of our calculation.

The comparison of temperature at 30 km depth indicates that the hottest lithosphere is located in the rift basins in NCC and Shanxi-Shanxi rift. The lithosphere beneath the Ordos block is hot in the east and cold in the west. The Taihang orogenic belt is in a transitional state.

Fig. 9 shows the distribution of the lithospheric thickness calculated for individual secondary massifs beneath the NCC. Fig. 10 shows the distribution of the lithospheric thickness beneath the NCC, as derived by Chen (2010) using seismic waves. A comparison between these two results indicates that the agreement is relatively good. For example, both show that there is a giant, thick lithosphere with a thickness of approximately 150 km in the bordering area between the north margin of the Taihang orogenic belt and the Yanshan orogenic belt, as indicated in Fig. 9. A significant difference between these two figures is that, in the figure of Chen, a 200-km-thick lithosphere can be found in the Lishi fault zone of the Luliang Mountains, where no low anomaly in the surface heat flow is observed (most likely due to the limited number of measurement sites for surface heat flow), resulting in the absence of this lithospheric data in our computation results.

As implied by the average thickness of the lithosphere beneath the NCC and the lithospheric thickness of the secondary massifs obtained above, the results of our calculations support the point of view that the lithosphere beneath the NCC has experienced thinning. The computation results of this study indicate that the average lithospheric thickness of the current NCC and the average thickness of the eastern NCC were 101 and 75 km, the average lithospheric thickness of the Ordos block is 141 km, that were thinner than that in the Archean era (200 km) by approximately 100, 125 and 60 km.
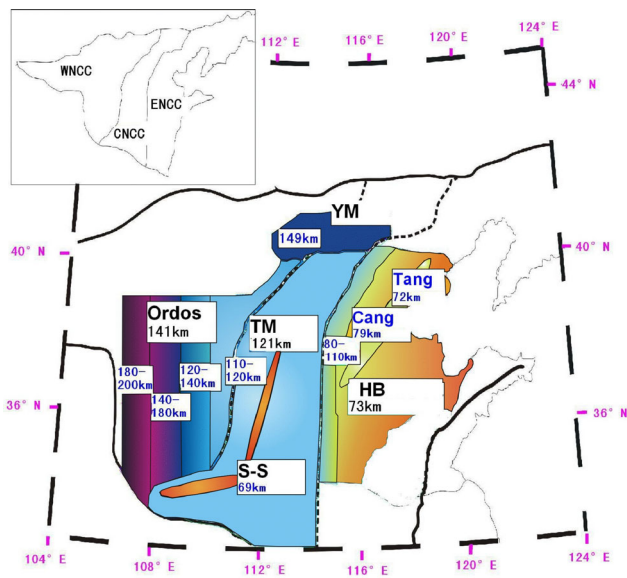
Figure 9. North China Craton lithosphere thickness distribution. HB, Hebei depression; Cang, Cangxian uplift; Tang, Tangshan earthquake region; TM, Taihang orogenic belt; YM, Yan Moutains orogenic belt; S-S, Fenwei graben; Ordos, Ordos block.
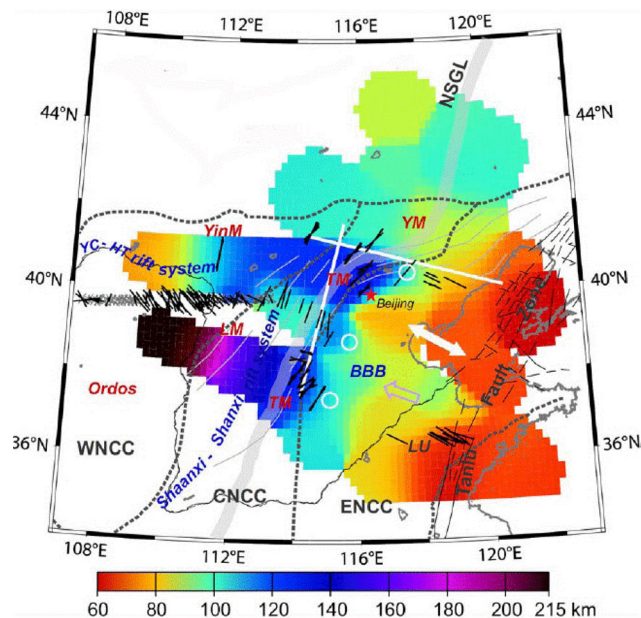

Figure 10. Lithosphere thickness map of NCC obtained by seismic survey (Chen 2010).

However, controversy remains regarding the temporal and spatial range of thinning, as well as the thinning mechanism (Gao *et al.* 1998; Menzies & Xu 1998; Xu 2001; Gao *et al.* 2004). As for the spatial extent of thinning, it is currently believed that the thinning process only occurred in the area in the east of the Taihang Mountains (Gao *et al.* 2002; Zheng *et al.* 2007; Xu *et al.* 2008). However, according to the computation results of this study, the Taihang orogenic belt and the Ordos block also underwent varying degrees of thinning, and the centre of thinning is along the north–south direction, consistent with that in the east of the NCC, along the Tanlu fault zone. This raises the question, does this indicate that the mid-west NCC experienced a thinning process that was controlled by the same mechanism as that in the east NCC?
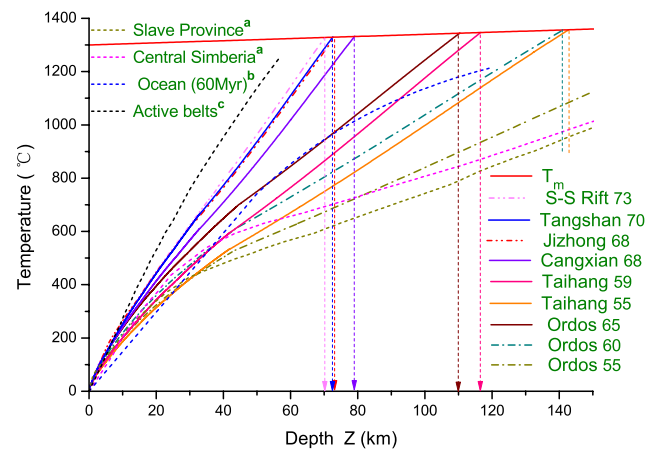

Figure 11. Depth–temperature relation of the NCC subblocks and comparison with other regions. Numbers were surface heat flow densities. [a]McKenzie *et al.* (2005), [b]Turcotte & Schubert (2002), [c]Hyndman *et al.* (2005).

4.6 The depth–temperature relation in secondary massifs

Fig. 11 shows the temperature–depth profile obtained through the calculation for individual secondary massifs beneath the NCC. Table 6 provides the parameters of the polynomial fit for the depth–temperature relationship in each secondary massif. The fitting equation is:

$$T = B_0 + B_1 h + B_2 h^2 + B_3 h^3 + B_4 h^4 + B_5 h^5, \tag{9}$$

where the unit of *T* is °C, and the unit of *h* is km. For comparison, in Fig. 11, we also plot the geothermal-depth profile for the Slave Province region of the Canadian Shield, the central region of the Siberian Shield (McKenzie *et al.* 2005), the 60-Myr oceanic lithosphere (Turcotte & Schubert (2002)) and the active orogenic belts (Hyndman *et al.* 2005). As shown in Fig. 11, the eastern region shows geothermal condition that is closer to that in the active orogenic belt, and the central region shows geothermal condition that is similar to that in the oceanic lithosphere. In contrast, the midwestern Ordos block shows geothermal condition that is close to that of the ancient craton.

5 CONCLUSIONS

In this study, the thermal diffusivity, specific heat capacity, weight-loss and thermal expansion coefficient under high temperature were measured for lherzolite beneath the NCC, and then we computed the temperature dependence of the lattice thermal conductivity for lherzolite under high temperature. Based on the dependence relationship derived between the lattice thermal conductivity and temperature under high temperature, as well as the surface heat flow, we iteratively calculated the average lithospheric thickness beneath the NCC and the lithospheric thickness in each secondary massif. The influence of radiative heat conduction on the thermal conductivity under high temperature and the pressure effect were taken into account during our calculation. Additionally, we derived the relationship between depth and temperature beneath the NCC and individual secondary massifs. The computation results for the lithospheric thickness are highly consistent with the results derived from the geophysical observations. The computation results of this study indicate that the average lithospheric thickness of the current NCC and the average thickness of the eastern NCC were 101 and 75 km,

Table 6. Quintic polynomial fitting coefficients of the depth–temperature relations of NCC subblocks. The unit of temperature is °C.

Subblocks	q_0 (mWm^{-2})	B_0	B_1	B_2 ($\times 10^{-1}$)	B_3 ($\times 10^{-3}$)	B_4 ($\times 10^{-6}$)	B_5 ($\times 10^{-9}$)
Hebei	68	15.078	30.764	−7.5378	18.981	−234.66	1143.55
Cangxian	68	20.081	25.871	−4.4782	8.3232	−71.991	250.269
Tangshan	70	17.622	26.589	−3.8500	7.2619	−72.6297	325.685
Taihang	59	21.904	19.678	−2.1694	1.9704	−5.88778	−2.29168
	55	20.908	18.419	−2.2274	2.0733	−8.01156	9.27015
S-S	73	18.744	28.843	−6.0218	15.216	−188.341	923.513
Ordos	65	24.520	24.287	−3.6630	4.9004	−34.8279	103.128
	60	25.393	21.751	−3.0155	3.0228	−14.1148	24.8647
	55	25.504	19.676	−2.8333	2.6337	−11.4119	18.6426

the lithospheric thickness of the Ordos block increases from 110 km in the east to approximately 200 km in the west, and the average thickness is 141 km, that were thinner than that in the Archean era (200 km) by approximately 100, 125 and 60 km. The results of our calculation support the view that the eastern NCC has experienced thinning. Further, our results indicate that the Taihang orogenic belt and Ordos block also have experienced varying degrees of thinning, where the centre of thinning is nearly along the north–south direction, consistent with the direction of the thinning centre in the eastern craton along the Tanlu fault zone. This phenomenon indicates that the mid-west NCC might have experienced a thinning process controlled by the same mechanism as that in the east NCC.

REFERENCES

Artemieva, I.M. & Mooney, W.D., 2001. Thermal thickness and evolution of Precambrian lithosphere: a global study, *J. geophys. Res.,* **106,** 16 387–16 414.

Brady, R.J., Ducea, M.N., Kidder, S.B. & Saleeby, J.B., 2006. The distribution of radiogenic heat production as a function of depth in the Sierra Nevada Batholith, California, *Lithos,* **86,** 229–244.

Chapman, D.S., 1986. Thermal gradients in the continental crust, *Geol. Soc. Spec. Publ.,* **24,** 63–70.

Chen, L., 2010. Concordant structural variations from the surface to the base of the upper mantle in the North China Craton and its tectonic implications, *Lithos,* **120,** 96–115.

Chen, L., Cheng, C. & Wei, Z., 2009. Seismic evidence for significant lateral variations in lithospheric thickness beneath the central and western North China Craton, *Earth planet. Sci. Lett.,* **286,** 171–183.

Chen, L., Tao, W., Zhao, L. & Zheng, T.Y., 2008. Distinct lateral variation of lithospheric thickness in the northeastern North China Craton, *Earth planet. Sci. Lett.,* **267,** 56–68.

Chen, L., Zheng, T.Y. & Xu, W.W., 2006. A thinned lithospheric image of the Tanlu Fault Zone, eastern China: constructed from wave equation based receiver function migration, *J. geophys. Res.,* **111,** B09312, doi:10.1029/2005JB003974.

Chi, Q. H., Yan & M. C., 1998. Radioactive elements of rocks in North China platform and the thermal structure and temperature distribution of the modern continental lithosphere, *Chin. J. Geophys.,* **41,** 38–48.

Deng, J.F., Su, S.G., Niu, Y.L., Liu, C., Zhao, G.C., Zhao, X.G., Zhou, S. & Wu, Z.X., 2007. A possible model for the lithospheric thinning of North China Craton: evidence from the Yanshanian (Jura-Cretaceous) magmatism and tectonism, *Lithos,* **96,** 22–35.

Fan, Q.C. & Hooper, P.R., 1989. The mineral chemistry of ultramafic xenoliths of eastern China—implications for upper mantle composition and the paleogeotherms, *J. Petrol.,* **30,** 1117–1158.

Fan, W.M., Zhang, H.F., Baker, J., Jarvis, K.E., Mason, P.R.D. & Menzies, M.A., 2000. On and off the North China Craton: where is the Archaean keel? *J. Petrol.,* **41,** 933–950.

Forster, A. & Forster, H.J., 2000. Crustal composition and mantle heat flow: implications from surface heat flow and radiogenic heat production in the Variscan Erzgebirge (Germany), *J. geophys. Res.,* **105,** 27 917–27 938.

Furlong, K.P. & Chapman, D.S., 1987. Crustal heterogeneities and the thermal structure of the continental crust, *Geophys. Res. Lett.,* **14,** 314–317.

Furlong, K.P. & Chapman, D.S., 2013. Heat flow, heat generation, and the thermal state of the lithosphere, *Annu. Rev. Earth planet. Sci.,* **41,** 385–410.

Gao, S., Zhang, B.R., Jin, Z.M., Kern, H., Luo, T.C. & Zhao, Z.D., 1998. How mafic is the lower continental crust? *Earth planet. Sci. Lett.,* **161,** 101–117.

Gao, S., Rudnick, R.L., Carlson, R.W., McDonough, W.F. & Liu, Y.S., 2002. Re-Os evidence for replacement of ancient mantle lithosphere beneath the North China craton, *Earth planet. Sci. Lett.,* **198,** 307–322.

Gao, S. *et al.*, 2004. Recycling lower continental crust in the North China craton, *Nature,* **432,** 892–897.

Gibert, B., Seipold, U., Tommasi, A. & Mainprice, D., 2003. Thermal diffusivity of upper mantle rocks: influence of temperature, pressure, and the deformation fabric, *J. geophys. Res.,* **108**(B8), 2359, doi:10.1029/2002JB002108.

Griffin, W.L., Andi, Z., O'Reilly, S.Y. & Ryan, C.G., 1998. Phanerozoic evolution of the lithosphere beneath the Sino-Korean Craton, in *Mantle Dynamics and Plate Interactions in East Asia,* pp. 107–126, eds Flower, M.F.J., Chung, S.L., Lo, C.H. & Lee, T.Y., American Geophysical Union.

Gualtieri, A.F., Giacobbe, C. & Viti, C., 2012. The dehydroxylation of serpentine group minerals, *Am. Mineral.,* **97,** 666–680.

Hasterok, D. & Chapman, D.S., 2011. Heat production and geotherms for the continental lithosphere, *Earth planet. Sci. Lett.,* **307,** 59–70.

He, L., Hu, S., Huang, S., Yang, W., Wang, J., Yuan, Y. & Yang, S., 2008. Heat flow study at the Chinese Continental Scientific Drilling site: borehole temperature, thermal conductivity, and radiogenic heat production, *J. geophys. Res.,* **113,** B02404, doi:10.1029/2007JB004958.

Hirono, T. & Hamada, Y., 2010. Specific heat capacity and thermal diffusivity and their temperature dependencies in a rock sample from adjacent to the Taiwan Chelungpu fault, *J. geophys. Res.,* **115,** B05313, doi:10.1029/2009JB006816.

Hofmeister, A.M., 1999. Mantle values of thermal conductivity and the geotherm from phonon lifetimes, *Science,* **283,** 1699–1706.

Hofmeister, A.M., 2006. Thermal diffusivity of garnets at high temperature, *Phys. Chem. Miner.,* **33,** 45–62.

Hofmeister, A.M., 2012. Thermal diffusivity of orthopyroxenes and protoenstatite as a function of temperature and chemical composition, *Eur. J. Mineral.,* **24,** 669–681.

Hofmeister, A.M. & Pertermann, M., 2008. Thermal diffusivity of clinopyroxenes at elevated temperature, *Eur. J. Mineral.,* **20,** 537–549.

Hu, S., He, L. & Wang, J., 2000. Heat flow in the continental area of China: a new data set, *Earth planet. Sci. Lett.,* **179,** 407–419.

Hu, S.B., He, L.J. & Wang, J.Y., 2001. Compilation of heat flow data in the China continental area (3rd edition), *Chinese J. Geophys,* **44,** 611–626 (in Chinese with English absract).

Huang, J. & Zhao, D., 2004. Crustal heterogeneity and seismotectonics of the region around Beijing, China, *Tectonophysics,* **385,** 159–180.

Huang, J. & Zhao, D., 2006. High-resolution mantle tomography of China and surrounding regions, *J. geophys. Res.,* **111,** B09305, doi:10.1029/2005JB004066.

Hunt, S.A., Walker, A.M., McCormack, R.J., Dobson, D.P., Wills, A.S. & Li, L., 2011. The effect of pressure on thermal diffusivity in pyroxenes, *Mineral. Mag.,* **75,** 2597–2610.

Hyndman, R.D., Currie, C.A. & Mazzotti, S.P., 2005. Subduction zone backarcs, mobile belts, and orogenic heat, *GSA Today,* **15,** 4–10.

Jaupart, C., Mareschal, J.C., Guillou-Frottier, L. & Davaille, A., 1998. Heat flow and thickness of the lithosphere in the Canadian Shield, *J. geophys. Res.,* **103,** 15 269–15 286.

Jia, S.X. & Zhang, X.K., 2005. Crustal structure and comparison of different tectonic blocks in North China, *Chin. J. Geophys.,* **48,** 672–683 (in Chinese with English absract).

Katsura, T., 1995. Thermal-diffusivity of olivine under upper-mantle conditions, *Geophys. J. Int.,* **122,** 63–69.

Ketcham, R.A., 1996. Distribution of heat-producing elements in the upper and middle crust of southern and west central Arizona: evidence from the core complexes, *J. geophys. Res.,* **101,** 13 611–13 632.

Lachenbruch, A.H., 1968. Preliminary geothermal model of the Sierra Nevada, *J. geophys. Res.,* **73,** 6977–6989.

Li, S., Mooney, W.D. & Fan, J., 2006. Crustal structure of mainland China from deep seismic sounding data, *Tectonophysics,* **420,** 239–252.

Ma, X., Liu, C. & Liu, G., 1991. Xiangshui (Jiangsu province) to Mandal (Nei Monggol) geoscience transect, *Acta Geol. Sin,* **3,** 199–215 (in Chinese with English absract).

McKenzie, D., Jackson, J. & Priestley, K., 2005. Thermal structure of oceanic and continental lithosphere, *Earth planet. Sci. Lett.,* **233,** 337–349.

Menzies, M.A. & Xu, Y.G., 1998. Geodynamics of the North China Craton, in *Mantle Dynamics and Plate Interactions in East Asia,* pp. 155–165, eds Flower, M.F.J., Chung, S.L., Lo, C.H. & Lee, T.Y., American Geophysical Union.

Merriman, J.D., Whittington, A.G., Hofmeister, A.M., Nabelek, P.I. & Benn, K., 2013. Thermal transport properties of major Archean rock types to high temperature and implications for cratonic geotherms, *Precambrian Res.,* **233,** 358–372.

Nabelek, P.I., Whittington, A.G. & Hofmeister, A.M., 2010. Strain heating as a mechanism for partial melting and ultrahigh temperature metamorphism in convergent orogens: implications of temperature-dependent thermal diffusivity and rheology, *J. geophys. Res.,* **115,** B12417, doi:10.1029/2010JB007727.

Nyblade, A.A. & Pollack, H.N., 1993. A global analysis of heat flow from Precambrian terrains: implications for the thermal structure of Archean and Proterozoic lithosphere, *J. geophys. Res.,* **98,** 12 207–12 218.

Osako, M., Ito, E. & Yoneda, A., 2004. Simultaneous measurements of thermal conductivity and thermal diffusivity for garnet and olivine under high pressure, *Phys. Earth planet. Inter.,* **143,** 311–320.

Pertermann, M. & Hofmeister, A.M., 2006. Thermal diffusivity of olivine-group minerals at high temperature, *Am. Mineral.,* **91,** 1747–1760.

Pertermann, M., Whittington, A.G., Hofmeister, A.M., Spera, F.J. & Zayak, J., 2008. Transport properties of low-sanidine single-crystals, glasses and melts at high temperature, *Contrib. Mineral. Petrol.,* **155,** 689–702.

Pinet, C. & Jaupart, C., 1987. The vertical distribution of radiogenic heat production in the Precambrian crust of Norway and Sweden: geothermal implications, *Geophys. Res. Lett.,* **14,** 260–263.

Poulier, C., Smith, D.S. & Absi, J., 2007. Thermal conductivity of pressed powder compacts: tin oxide and alumina, *J. Eur. Ceram. Soc.,* **27,** 475–478.

Qiu, R.Z., Deng, J.F., Zhou, S., Li, J.F., Xiao, Q.H., Wu, Z.X. & Liu, C., 2005. Lithosphere types in North China: evidence from geology and geophysics, *Sci. China Ser. D: Earth Sci.,* **48,** 1809–1827 (in Chinese with English absract).

Romine, W., Whittington, A., Nabelek, P. & Hofmeister, A., 2012. Thermal diffusivity of rhyolitic glasses and melts: effects of temperature, crystals and dissolved water, *Bull. Volcanol.,* **74,** 2273–2287.

Roy, R.F., Blackwell, D.D. & Birch, F., 1968. Heat generation of plutonic rocks and continental heat flow provinces, *Earth planet. Sci. Lett.,* **5,** 1–12.

Roy, S., Ray, L., Bhattacharya, A. & Srinivasan, R., 2008. Heat flow and crustal thermal structure in the Late Archaean Closepet Granite batholith, south India, *Int. J. Earth Sci.,* **97,** 245–256.

Rudnick, R.L., McDonough, W.F. & O'Connell, R.J., 1998. Thermal structure, thickness and composition of continental lithosphere, *Chem. Geol.,* **145,** 395–411.

Saxena, 1996. Earth mineralogical model: Gibbs free energy minimization computation in the system MgO-FeO-SiO$_2$, *Geochim. Cosmochim. Acta,* **60,** 2379–2395.

Seipold, U. & Schilling, F.R., 2003. Heat transport in serpentinites, *Tectonophysics,* **370,** 147–162.

Shen, H., Xu, J.Y., Wu, A.H., Zhao, J.T. & Shi, M.L., 2009. Magnetic and thermal properties of perovskite YFeO$_3$ single crystals, *Mat. Sci. Eng. B-Solid,* **157,** 77–80.

Smith, D.S., Grandjean, S., Absi, J., Kadiebu, S. & Fayette, S., 2003. Grain-boundary thermal resistance in polycrystalline oxides: alumina, tin oxide, and magnesia, *High Temp.-High Pres.,* **35–36,** 93–99.

Thompson, A.B., 1992. Water in the Earth's upper mantle, *Nature,* **358,** 295–302.

Tommasi, A., Gibert, B., Seipold, U. & Mainprice, D., 2001. Anisotropy of thermal diffusivity in the upper mantle, *Nature,* **411,** 783–786.

Turcotte, D. & Schubert, G., 2002. *Geodynamics,* 2nd edition, pp. 291, Cambridge University Press.

Wang & Huang, 1990. Compilation of heat flow data in the China continental area, *Seismol. Geol.,* **12,** 351–366 (in Chinese with English abstract).

Wang, Y. & Cheng, S.H., 2012. Lithospheric thermal structure and rheology of the eastern China, *J. Asian Earth Sci.,* **47,** 51–63.

Xu, P.F. & Zhao, D.P., 2009. Upper-mantle velocity structure beneath the North China Craton: implications for lithospheric thinning, *Geophys. J. Int.,* **177,** 1279–1283.

Xu, Y.G., 2001. Thermo-tectonic destruction of the archaean lithospheric keel beneath the Sino-Korean Craton in China: evidence, timing and mechanism, *Phys. Chem. Earth Part A–Solid Earth Geod.,* **26,** 747–757.

Xu, Y.G., Blusztajn, J., Ma, J.L., Suzuki, K., Liu, J.F. & Hart, S.R., 2008. Late Archean to Early Proterozoic lithospheric mantle beneath the western North China Craton: Sr–Nd–Os isotopes of peridotite xenoliths from Yangyuan and Fansi, *Lithos,* **102,** 25–42.

Xu, Y.S., Shankland, T.J., Linhardt, S., Rubie, D.C., Langenhorst, F. & Klasinski, K., 2004. Thermal diffusivity and conductivity of olivine, wadsleyite and ringwoodite to 20 GPa and 1373 K, *Phys. Earth planet. Inter.,* **143,** 321–336.

Zang, S.X., Liu, Y.G. & Ning, J.Y., 2002. Thermal structure of the lithosphere in North China, *Chinese J. Geophys.,* **45,** 56–66 (in Chinese with English abstract).

Zheng, T.Y., Chen, L., Zhao, L. & Zhu, R.X., 2007. Crustal structure across the Yanshan belt at the northern margin of the North China Craton, *Phys. Earth planet. Inter.,* **161,** 36–49.

Zheng, Y., Shen, W.S., Zhou, L.Q., Yang, Y.J., Xie, Z.J. & Ritzwoller, M.H., 2011. Crust and uppermost mantle beneath the North China Craton, northeastern China, and the Sea of Japan from ambient noise tomography, *J. geophys. Res.,* **116,** B12312, doi:10.1029/2011JB008637.

Zivcova, Z., Gregorova, E., Pabst, W., Smith, D.S., Michot, A. & Poulier, C., 2009. Thermal conductivity of porous alumina ceramics prepared using starch as a pore-forming agent, *J. Eur. Ceram. Soc.,* **29,** 347–353.